Contribution of AMOC Decline to Uncertainty in Global Warming via Ocean Heat Uptake and Climate Feedbacks

Lily C. Hahn,[a] Nicholas J. Lutsko,[a] Ian Eisenman,[a] Matthew T. Luongo,[a,b] Shang-Ping Xie[a]

[a] *Scripps Institution of Oceanography, San Diego, CA*

[b] *Cooperative Institute for Climate, Ocean, and Ecosystem Studies & School of Oceanography, University of Washington, Seattle, WA*

Corresponding author: Lily C. Hahn, lihahn@ucsd.edu

ABSTRACT

Climate models vary widely in projections of 21st century global warming and projections of the Atlantic Meridional Overturning Circulation (AMOC). However, the extent to which this uncertainty in AMOC contributes to uncertainty in warming has not yet been quantified. To investigate this, we perform climate model experiments that increase CO_2 concentrations while imposing the range of AMOC declines found in the Coupled Model Intercomparison Project Phase 6 (CMIP6). We find that intermodel spread in the AMOC decline, imposed within a single model, reproduces 20% of the total intermodel spread in global warming. An idealized energy-balance model indicates that changes in ocean heat uptake and climate feedbacks contribute approximately equally to enhanced warming in our experiment with a smaller AMOC decline. A smaller AMOC decline produces greater ocean-to-atmosphere heating in the North Atlantic, which increases near-surface warming and reduces the lower-tropospheric stability to produce less-negative lapse-rate and shortwave cloud feedbacks. In the northern tropics, surface warming is enhanced by the wind-evaporation-SST feedback and by more-positive longwave cloud and water vapor feedbacks due to a northward shift of the Intertropical Convergence Zone. A Green's function analysis confirms that a less-negative global feedback with a smaller AMOC decline is predominantly driven by sea-surface warming in the extratropical North Atlantic. Spread in the AMOC decline is correlated with similar differences in ocean heat uptake and climate feedbacks across CMIP6 models as in our experiments. These results suggest that model uncertainty in global warming may be substantially reduced by constraining projections of AMOC.

1. Introduction

Projected 21st century global warming varies by more than a factor of two in the latest generation of climate models participating in the Coupled Model Intercomparison Project Phase 6 (CMIP6; IPCC AR6). A central goal of climate science is to constrain this spread in the modeled climate response by better understanding and predicting the processes that contribute to it. Intermodel spread in transient warming is driven not only by uncertainty in radiative forcing and climate feedbacks, but also by uncertainty in ocean heat uptake (Geoffroy et al., 2012; Gregory and Mitchell, 1997; Gregory and Forster, 2008; Gregory et al., 2024; Lutsko and Popp, 2019; Raper et al., 2002). In particular, transient warming is sensitive to the strength of the Atlantic Meridional Overturning Circulation (AMOC), a system of ocean currents characterized by northward flowing surface waters and deep sinking in the subpolar North Atlantic. Models robustly project a decline in the AMOC under increased CO_2 forcing, with a larger decline in models that simulate a stronger present-day AMOC (Figure 1a,b; Gregory et al., 2005; Weijer et al., 2020). However, there is considerable intermodel spread in the strength of the mean-state AMOC and the degree of its decline (Figure 1a,b; Bellomo et al., 2021). In CMIP6 models under abrupt CO_2 quadrupling, this decline ranges from 17 to 82% of the mean-state strength (Figure S1).

Past studies indicate a significant effect of the present-day AMOC (Kostov et al., 2014; He et al., 2017) and its decline (Liu et al., 2020; Rugenstein et al., 2013; Vellinga and Wood, 2008; Winton et al., 2013) on transient warming. Using idealized model experiments with CO_2 concentrations rising at 1% per year, Trossman et al. (2016) estimate that at the time of CO_2 doubling, a 25% decline in AMOC reduces global-mean surface warming by 20%. In CMIP6, models with a weak mean-state AMOC tend to have a weak AMOC decline (r^2=0.53) and large global-mean warming (r^2=0.24) under increased CO_2 forcing (Figure 1; regressions calculated for averages over years 85-115 of *abrupt-4xCO2* simulations). However, these CMIP6 experiments include many other factors that influence intermodel spread in transient warming, making it difficult to isolate the role of AMOC and its decline. It is unclear how the effects of AMOC modeled in idealized experiments scale to the range of intermodel spread found across CMIP6 models: the contribution of uncertainty in AMOC to uncertainty in global transient warming has not yet been quantified.

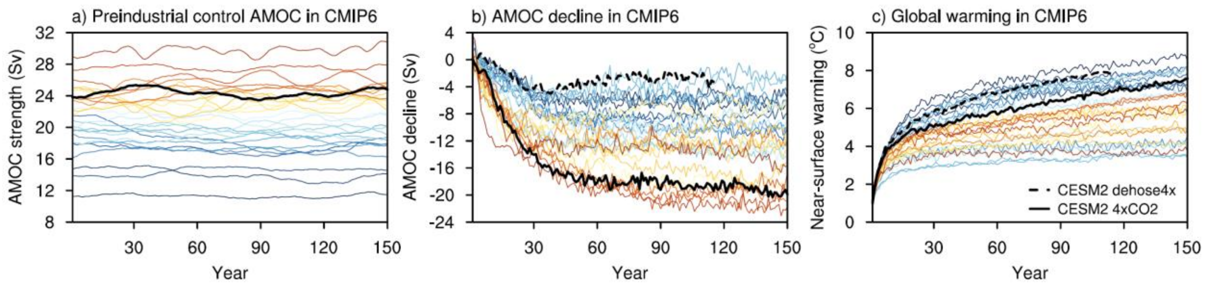

Figure 1. Intermodel spread across 28 CMIP6 models in (a) the AMOC strength (Sv) in a preindustrial control experiment (*piControl*); and (b) the AMOC decline (Sv) and (c) global-mean near-surface warming (°C) in an abrupt CO_2 quadrupling experiment (*abrupt-4xCO2*) compared to the *piControl* experiment. Models are sorted from weakest (blue lines) to strongest (red lines) *piControl* AMOC strength, which is calculated as the maximum in the ocean meridional overturning mass streamfunction in the Atlantic north of 30˚N and at depth greater than 500 m (e.g., Liu et al., 2020). The CESM2 CMIP6 simulations (solid black lines) and our CESM2 dehosing experiment (dashed black lines) are overlaid.

AMOC mediates the rate and pattern of ocean heat uptake, which can impact global warming both directly and by changing the global climate feedback. Specifically, the AMOC decline may impact the global feedback by preferentially cooling the Northern Hemisphere high latitudes, a region with strong amplifying feedbacks (Armour et al., 2013; Bitz et al., 2012; Marshall et al., 2015; Winton et al., 2010, 2013), or by changing local feedbacks themselves (Rose et al., 2014; Winton, 2003). Past studies point to a key role for the shortwave cloud feedback: when cloud feedbacks are held fixed, the global cooling response to the AMOC decline is reduced by 30-60% (He et al., 2017; Trossman et al., 2016; Zhang et al., 2010). However, the extent to which the AMOC decline impacts other climate feedbacks, the mechanisms of this feedback response, and this response's robustness and contribution to the spread across the latest generation of climate models remains to be explored.

To quantify and mechanistically investigate the role of model uncertainty in AMOC for uncertainty in near-future warming, we use novel experiments that impose the CMIP6 range in AMOC declines within a single climate model. We use an idealized energy-balance model to assess the relative role of changes in ocean heat uptake and atmospheric feedbacks for global warming in these experiments. Finding an important role for atmospheric feedback changes, we investigate what drives these changes and how they compare to AMOC-related feedback differences across climate models in CMIP6. Our results have direct implications for how constraining ocean circulation in climate models may improve projections of climate feedbacks and near-future warming.

2. CESM2 Experiments

a) Experimental design

We perform experiments with the fully-coupled Community Earth System Model Version 2 (CESM2) at a nominal 1° horizontal resolution (Danabasoglu et al., 2020). This model uses the Community Atmosphere Model Version 6 (CAM6), the Parallel Ocean Program Version 2 (POP2; Smith et al., 2010), the Los Alamos Sea Ice Model Version 5.1.2 (CICE5; Hunke et al., 2015), the Community Ice Sheet Model Version 2.1 (CISM2.1; Lipscomb et al., 2019), the Community Land Model Version 5 (CLM5; Lawrence et al., 2019), and the Model for Scale Adaptive River Transport (MOSART; H. Y. Li et al., 2013).

We use the CESM2 preindustrial control (*piControl*) and abrupt CO_2 quadrupling (*abrupt-4xCO2,* abbreviated here as *4xCO2)* experiments from the CMIP6 archive. The CESM2 *4xCO2* experiment has one of the largest AMOC declines of the CMIP6 models (solid black line, Figure 1b). To capture the range in AMOC declines across CMIP6, we perform an additional experiment in CESM2 (*dehose4x*) that abruptly quadruples CO_2 while simultaneously removing surface freshwater over the Arctic and north of 50°N in the North Atlantic. While traditional freshwater hosing experiments add a freshwater flux to the Northern Hemisphere high latitudes to simulate an AMOC decline, *dehose4x* removes freshwater to reduce the AMOC decline. We perturb the freshwater budget using a virtual salinity flux and apply a compensating salinity flux over the rest of the global ocean to maintain constant global salinity, using a spatial hosing pattern from the North Atlantic Hosing Model Intercomparison Project (NAHosMIP; Figure 1a in Jackson et al., 2023). The *dehose4x* experiment applies a constant -0.5 Sv freshwater flux to reproduce the smallest AMOC decline seen in CMIP6 (dashed black line, Figure 1b). We can then use the difference between the *dehose4x* and *4xCO2* experiments to assess how the CMIP6 spread in AMOC decline, imposed within a single model, impacts global warming. These experiments span most, but not all, of the CMIP6 spread in AMOC decline, as several models have a larger AMOC decline than CESM2; imposing the full spread may produce a larger impact on warming.

We run the *dehose4x* experiment for 115 years and show anomalies for the *dehose4x* – *4xCO2* experiments averaged over years 85-115. We run this experiment for a shorter period than the typical 150-year *4xCO2* experiments in CMIP6 to conserve computing resources, as

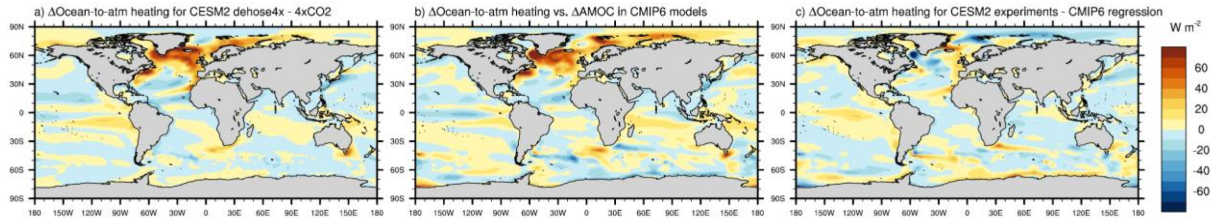

Figure 2. (a) Ocean-to-atmosphere heating anomaly in the CESM2 *dehose4x – 4xCO2* experiments; (b) ocean-to-atmosphere heating anomaly in the *abrupt4xCO2 – piControl* CMIP6 experiments, regressed against the anomaly in AMOC strength across CMIP6 models and scaled by the CESM2 *dehose4x – 4xCO2* anomaly in AMOC strength; and (c) the difference between panels a and b (W m^{-2}). All anomalies are averaged over years 85-115 after CO_2 quadrupling.

the intermodel spread in AMOC decline across CMIP6 models for years 85-115 captures most of the spread at year 150. We calculate anomalies during corresponding time periods between each CO_2 quadrupling experiment and a 21-year running average of *piControl* to account for model drift (Caldwell et al., 2016; Zelinka et al., 2020).

b) Impacts on ocean heat uptake compared to CMIP6

We first consider the extent to which these two experiments with a single model are representative of AMOC impacts across CMIP6 models. Specifically, do ocean heat uptake anomalies associated with AMOC differences in CESM2 resemble the spread in ocean heat uptake associated with AMOC differences across CMIP6 models? We diagnose differences in ocean-to-atmosphere heating for the *dehose4x – 4xCO2* experiments using net surface heat flux anomalies (Figure 2a). In comparison, we regress anomalies in ocean-to-atmosphere heating against anomalies in AMOC strength across CMIP6 models for the *4xCO2 – piControl* experiments, then scale this CMIP6 regression (in W m^{-2} Sv^{-1}) by the *dehose4x – 4xCO2* difference in AMOC strength (in Sv) to compare it with heating anomalies in the CESM2 experiments (in W m^{-2}; Figure 2b).

The pattern of heating anomalies in our CESM2 experiments is remarkably similar to that across CMIP6 models: a smaller AMOC decline (which results in a stronger AMOC) produces greater ocean-to-atmosphere heating in the subpolar and eastern subtropical North Atlantic (Figure 2a,b). Compared to CMIP6 models, the CESM2 experiments tend to produce less heating in the Arctic Ocean and Labrador Sea (Figure 2c). Some of this discrepancy may result from model differences in the location of deep ocean convection, which occurs in the Labrador Sea in CESM2 but elsewhere in many other models (Liu et al., 2024). Sea ice differences may also contribute to weaker ocean-to-atmosphere heating in the Arctic in the CESM2 experiments than in CMIP6 models. CESM2 has insufficient sea ice in *piControl*

(Kay et al., 2022) and very little sea ice by year-100 of either the CESM2 *4xCO2* or *dehose4x* experiments (not shown). In contrast, CMIP6 models with a weak AMOC decline tend to have a weak mean-state AMOC that supports more climatological sea ice. As a result, greater northward heat transport associated with the weaker AMOC decline in these models can produce larger sea-ice loss and increased ocean-to-atmosphere heating in the Arctic (Lin et al., 2023). There are additional, smaller differences in the North Atlantic between our CESM2 experiments and CMIP6 models. However, the impact of AMOC on ocean-to-atmosphere heating within CESM2 largely resembles the relationship between AMOC and ocean-to-atmosphere heating across CMIP6 models.

3. Impact of AMOC Decline on Global Warming

a) Global warming

Imposing the intermodel spread in AMOC decline within a single model produces a 1°C difference in global near-surface warming, which is more than 20% of the total intermodel spread in warming in CMIP6 (averaged over years 85-115 after CO_2 quadrupling; Figure 1c, black lines). A weaker AMOC decline in *dehose4x* compared to *4xCO2* warms the surface in the Northern Hemisphere, particularly at high latitudes, and slightly cools the Southern Hemisphere (Figure 3a). Regions with the largest ocean-to-atmosphere heating anomalies (Figure 2a), i.e. the subpolar North Atlantic, experience the largest surface warming, but many regions with negative ocean-to-atmosphere heating anomalies in the Northern Hemisphere still exhibit atmospheric warming. This opposite ocean heating and surface warming response suggests that ocean heat transport changes are a primary, but not sole, driver of enhanced surface warming with a stronger AMOC. Beyond ocean heating, surface warming may also be amplified by changes in atmospheric feedbacks.

b) Relative roles of ocean heat uptake and climate feedbacks for warming response to AMOC

Changes in both ocean heat uptake and climate feedbacks may contribute to larger near-future warming in experiments with a stronger AMOC. Since ocean heat uptake and climate feedbacks interact with each other, we would ideally use additional idealized experiments to disentangle the role of each. To this end, previous studies have shown that when cloud feedbacks are held fixed in a comprehensive climate model, the global cooling response to the AMOC decline is reduced by 30-60% (Trossman et al., 2016; Zhang et al., 2010). Here

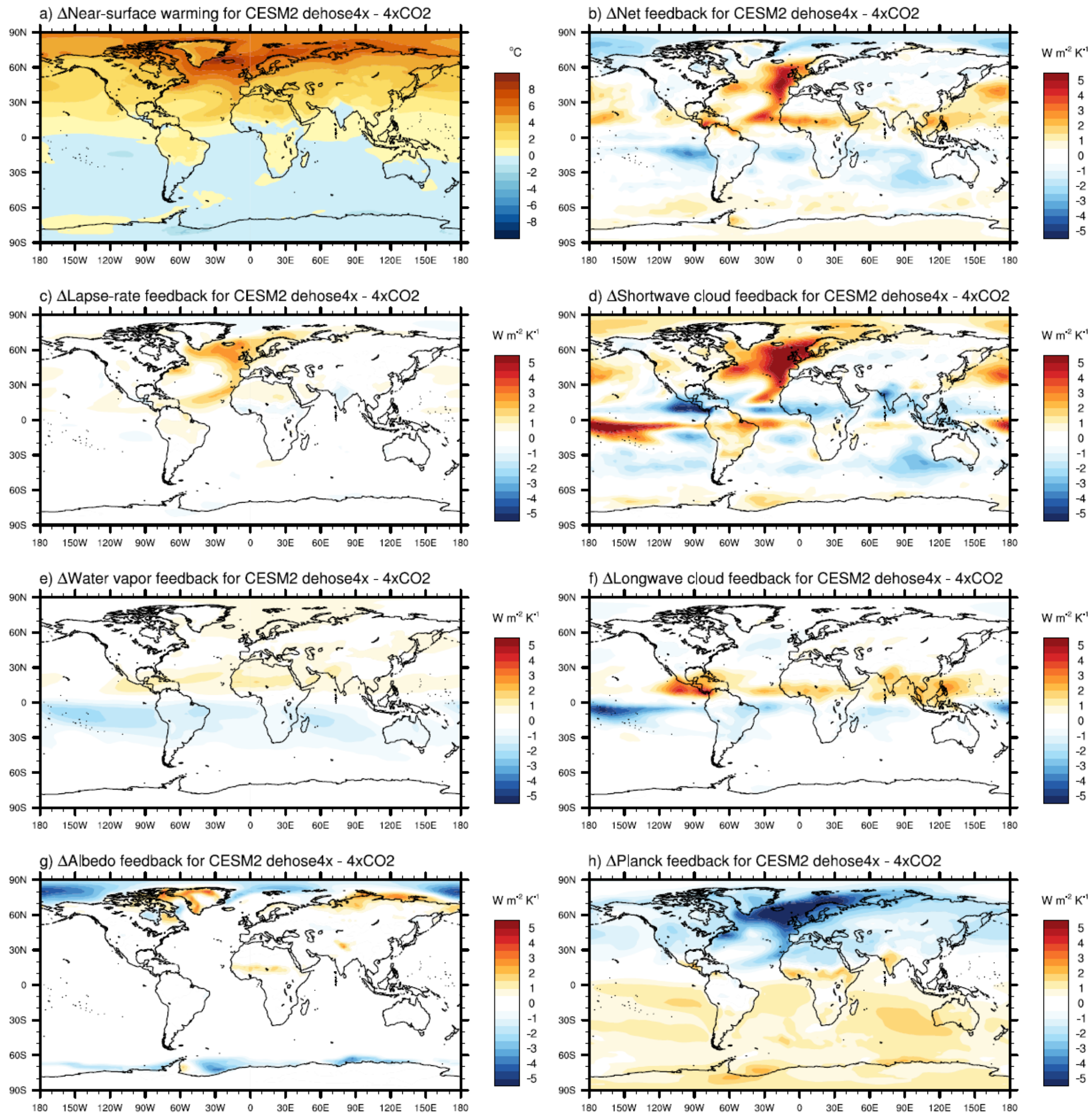

Figure 3. (a) Near-surface warming (°C) in the CESM2 *dehose4x* – *4xCO2* experiments, averaged over years 85-115 after CO_2 quadrupling. (b-h) Difference in climate feedbacks for *dehose4x* – *piControl* compared to *4xCO2* – *piControl* experiments for (b) the net feedback, (c) the lapse-rate feedback, (d) the shortwave cloud feedback, (e) the water vapor feedback, (f) the longwave cloud feedback, (g) the albedo feedback, and (h) the Planck feedback (W m^{-2} K^{-1}). Small residual term is shown in Figure S2a.

we investigate the relative role of ocean heat uptake and climate feedbacks using a simple energy balance model and leave additional climate model experiments for future work.

We use a zero-layer energy balance model (e.g., Gregory and Mitchell, 1997):

$$R = F + \lambda T = \kappa T \,, \quad (1)$$

where R and T are the global-mean anomalies in top-of-atmosphere (TOA) radiation and near-surface temperature, respectively, and anomalies are calculated for the *dehose4x* and

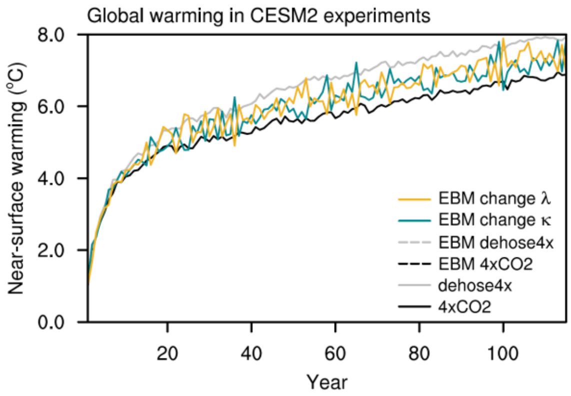

Figure 4. Near-surface, global-mean warming (°C) for *dehose4x – piControl* (solid grey) and *4xCO2 – piControl* (solid black) experiments, warming reconstructions using a single-layer energy-balance model (EBM; dashed grey and black), and reconstructed warming in the EBM using *4xCO2 – piControl* λ and *dehose4x – piControl* κ (turquoise), or using *4xCO2 – piControl* κ and *dehose4x – piControl* λ (yellow).

4xCO2 experiments in comparison with *piControl*. Given the small heat capacity of the atmosphere and ocean mixed layer, the anomaly in deep ocean heat uptake, κT, is approximately equal to the anomaly in TOA radiation, R. We use F = 9.74 W m^{-2} K^{-1}, the land-surface-corrected and tropospherically-corrected effective radiative forcing for abrupt CO_2 quadrupling in CESM2 (Table S1 in Smith et al., 2020), and calculate the net climate feedback, $\lambda = \frac{R - F}{T}$, and the ocean heat uptake efficiency, $\kappa = \frac{R}{T}$, both of which vary over time. In this model, radiative forcing F is balanced both by ocean heat uptake, κT, and by heat loss to space, λT.

We can use this model to exactly reconstruct $T = \frac{F}{\kappa - \lambda}$, the near-surface warming for *4xCO2-piControl* and *dehose4x-piControl* (Figure 4; overlapping dashed versus solid grey and black lines). We then isolate how feedback differences alone impact global near-surface warming by calculating T using κ from *4xCO2-piControl* and λ from *dehose4x-piControl* (Figure 4; yellow line). Similarly, we use λ from *4xCO2-piControl* and κ from *dehose4x-piControl* to isolate the effect of changes in ocean heat uptake alone (Figure 4; turquoise line). Averaged over years 85-115, ocean heat uptake explains 41% of the difference in warming for *dehose4x - 4xCO2*, while the global feedback explains 53% of this warming difference, with the remainder contributed by simultaneous changes in κ and λ. This simple model indicates that changes in ocean heat uptake and climate feedbacks contribute approximately equally to increased warming with a weaker AMOC decline.

c) Climate feedback decomposition

To understand how the AMOC decline influences the net climate feedback, we decompose this feedback into the albedo, Planck, lapse-rate, water vapor, and cloud feedbacks using the radiative kernel method described in Shell et al. (2008) and Soden et al. (2008). We calculate climate feedbacks in each CO_2 quadrupling experiment compared to the preindustrial control using a regression of local anomalies in top-of-atmosphere (TOA) radiation against the global-mean anomaly in near-surface temperature for the first 115 years after CO_2 quadrupling. We find similar results when quantifying feedbacks as the quotient of anomalies in TOA radiation and near-surface temperature averaged over years 85-115 (not shown). However, we show feedbacks calculated using regression rather than division to isolate temperature-mediated feedbacks and exclude rapid adjustments to forcing. We use radiative kernels derived from the ERA-Interim reanalysis by Huang et al. (2017), which produce a very small residual between the actual net feedback and the sum of the kernel-calculated feedbacks (Figure S2a)—slightly smaller than the residual produced by the CAM5 kernels (Pendergrass et al., 2018; not shown). We show feedbacks for *4xCO2 – piControl* in Figure S3, for *dehose4x - piControl* in Figure S4, and the difference between *dehose4x - piControl* and *4xCO2 – piControl* in Figure 3b-h.

A stronger AMOC in the *dehose4x* experiment produces a less-negative global feedback than in the *4xCO2* experiment (-0.62 versus -0.73 W m^{-2} K^{-1}). Regionally, the net feedback becomes less negative in the North Atlantic and North Pacific and becomes less positive to the south of the equator in the eastern tropical Pacific, Atlantic, and Indian Ocean (Figure 3b, Figure S3b, S4b). We first decompose the net feedback into individual feedback changes, and later evaluate the relative contributions of regional changes to the global feedback change using a Green’s functions approach (section 3g).

Changes in the net feedback are dominated by the shortwave cloud and lapse-rate feedbacks (Figure 3c,d): a stronger AMOC produces less-negative shortwave cloud and lapse-rate feedbacks, particularly in the North Atlantic. The shortwave cloud feedback also becomes less negative in the North Pacific and less positive in Southern Hemisphere stratocumulus cloud regions. We explore what drives these changes in the lapse-rate and shortwave cloud feedbacks in the next section.

Water vapor and longwave cloud feedbacks increase in the northern tropics and decrease in the southern tropics with a stronger AMOC (Figure 3e,f). This results from a northward shift of the Intertropical Convergence Zone (ITCZ) and associated high clouds and moisture in response to Northern Hemisphere warming and Southern Hemisphere cooling (Figure S5a-d; Zhang and Delworth, 2005; Kang et al., 2008). This northward shift of the ITCZ and high cloud cover produces compensating changes in longwave and shortwave cloud feedbacks in the deep tropics (Figure 3d,f). In addition to these dynamic effects, Northern Hemisphere warming and Southern Hemisphere cooling also support thermodynamic changes in the tropical water vapor feedback via Clausius-Clapeyron.

Albedo feedback differences are confined to polar regions: due to increased warming in *dehose4x*, the Arctic becomes ice-free sooner and produces a weaker Arctic albedo feedback than in *4xCO2*, which continues to lose sea ice throughout the experiment (Figure 3g). Slight cooling in the Antarctic with a stronger AMOC sustains sea ice and weakens the Antarctic albedo feedback. Lastly, the Planck feedback opposes warming anomalies globally (Figure 3h).

d) Drivers of changes in cloud and lapse-rate feedbacks

To investigate how differences in AMOC induce differences in the shortwave low-cloud feedback, we use the cloud controlling factor (CCF) methodology of Myers et al. (2021). This analysis approximates the shortwave low-cloud feedback, $\lambda_{swcld,low}$, as the sum of contributions from anomalies in local cloud controlling factors, x_i:

$$\lambda_{swcld,low} \equiv \frac{dR_{swcld,low}}{d\bar{T}} \approx \sum_i \frac{\delta R_{swcld,low}}{\delta x_i} \frac{dx_i}{d\bar{T}}, \quad (2)$$

where $R_{swcld,low}$ is the local anomaly in TOA radiation induced by low clouds and $\bar{T}$ is the global-mean near-surface temperature anomaly. As in our standard feedback calculations, anomalies are calculated for *dehose4x – piControl* and *4xCO2 – piControl*. We use 6 cloud-controlling factors (x_i), as defined in Myers et al. (2021): sea-surface temperature (SST), estimated inversion strength (EIS), horizontal surface temperature advection (T_{adv}), relative humidity at 700 hPa (RH_{700}), vertical velocity at 700 hPa (ω_{700}), and near-surface wind speed (WS). We regress anomalies in cloud controlling factors against anomalies in global-mean near-surface temperature ($\frac{dx_i}{d\bar{T}}$) for the first 115 years after CO_2 quadrupling in our experiments, and use cloud radiative sensitivities ($\frac{\delta R_{swcld,low}}{\delta x_i}$) that have been calculated for

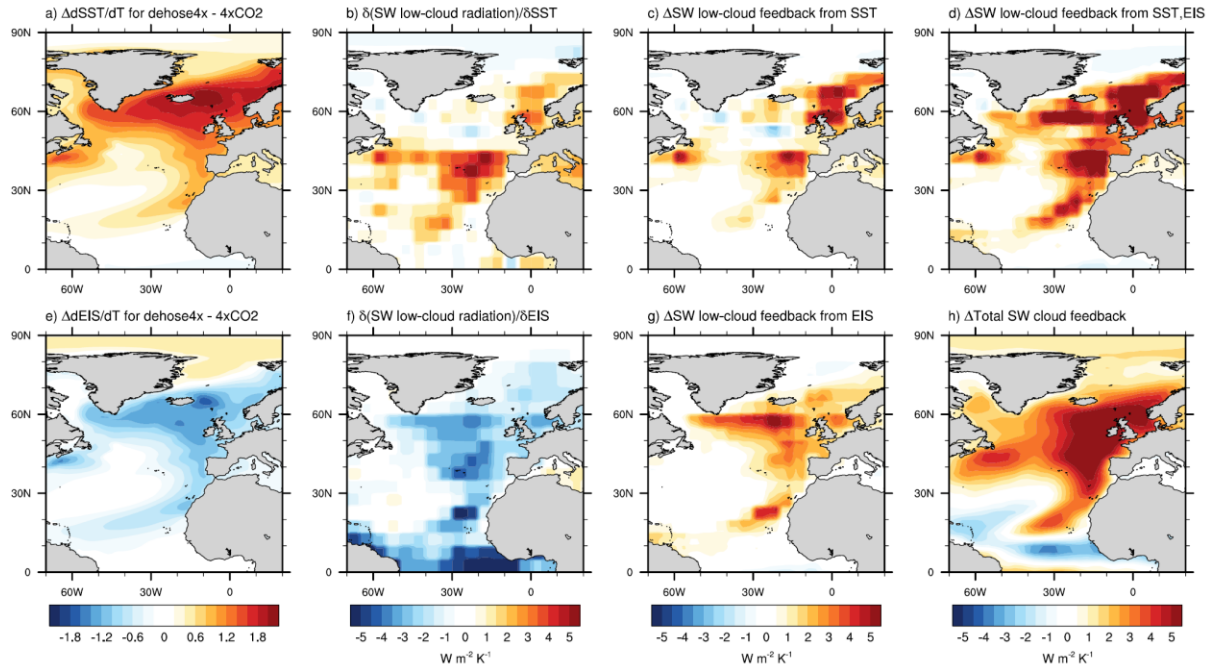

Figure 5. Differences in cloud-controlling factor sensitivity to global-mean warming, (a) $\Delta\frac{dSST}{d\bar{T}}$ and (e) $\Delta\frac{dEIS}{d\bar{T}}$, for *dehose4x - 4xCO2* experiments; sensitivity of low-cloud-induced shortwave TOA radiation anomalies to anomalies in (b) SST and (f) EIS (W m^{-2} K^{-1}); contribution of (c) SST, (g) EIS, and (d) both SST and EIS to the difference in shortwave low-cloud feedback for *dehose4x - 4xCO2* (W m^{-2} K^{-1}); and (h) the total difference in shortwave cloud feedback for *dehose4x - 4xCO2* from radiative kernel analysis (W m^{-2} K^{-1}).

CESM2 by Kang et al. (2023) using ridge regression (Ceppi et al., 2021). For comparison, we also use observationally-derived cloud radiative sensitivities from Myers et al. (2021).

A stronger AMOC in the *dehose4x* experiment produces more North Atlantic sea-surface warming per degree of global warming (Figure 5a), which reduces the lower-tropospheric inversion strength (Figure 5e) and produces a more-positive lapse-rate feedback (Figure 3c). Warmer SSTs and a weaker surface inversion both reduce low cloud cover, allowing for more solar absorption in a more-positive shortwave low-cloud feedback (Figure 5c,g). These results support the hypothesis of Zhang et al. (2010) and Trossman et al. (2016) that a stronger AMOC reduces low cloud cover by reducing the lower tropospheric stability and enabling more entrainment of dry air from the upper troposphere to the lower troposphere (Klein and Hartmann, 1993; Wood and Bretherton, 2006). A stronger AMOC may also reduce low cloud cover by weakening the midlatitude jet (Figure S5e-g; Trossman et al., 2016) as a result of reducing the equator-to-pole temperature gradient in the Northern Hemisphere.

The cloud controlling factors SST and EIS largely reproduce the pattern and magnitude of AMOC-induced differences in the North Atlantic shortwave cloud feedback (Figure 5d,h), with very little contribution from other cloud-controlling factors (Figure S6). While the shortwave cloud feedback becomes more negative in some regions of the tropical North Atlantic (Figure 5h), the CCF-estimated low-cloud feedback shows little change here (Figure 5d). This more-negative shortwave cloud feedback is driven by high-cloud changes in response to a northward ITCZ shift, as evidenced by a compensating, co-located longwave cloud feedback (Figure 3f), which are not included in the CCF low-cloud analysis.

Cloud controlling factors also reproduce changes in the shortwave low-cloud feedback beyond the North Atlantic: warmer SSTs and reduced EIS in the North Pacific produce a more-positive feedback, while cooler SSTs and increased EIS in Southern Hemisphere stratocumulus regions produce a more-negative feedback (Figure S6s,t). These results are robust to substituting observed, rather than modeled, cloud radiative sensitivities, which again illustrate the dominant role of SST and EIS for the low-cloud response to the AMOC decline (Figure S7-10).

e) Mixed-layer heat budget and role of wind-evaporation-SST feedback

We have shown that the shortwave cloud feedback is highly sensitive to AMOC-induced changes in SST—but what produces these SST changes? Additionally, how does a stronger AMOC increase surface warming in other regions of the northern tropics that experience negative ocean-atmosphere heating anomalies? Section 3c demonstrates that this warming can be partly explained by a northward ITCZ shift and more-positive water vapor and longwave cloud feedbacks in the northern tropics. Here we explore additional factors that contribute to these SST changes using a mixed-layer heat budget (e.g., Luongo et al., 2023; Xie et al., 2010):

$$C\,\frac{\partial T'}{\partial t} = O' + Q'_{SW} + Q'_{LW} + Q'_{SH} + Q'_{LH}, \qquad (3)$$

where C is the effective heat capacity of the ocean mixed layer, and anomalies in SST (T') evolve in response to anomalies in net surface heat fluxes, including shortwave (Q'_{SW}) and longwave radiation (Q'_{LW}) and sensible (Q'_{SH}) and latent heat fluxes (Q'_{LH}), as well as the effect of anomalous ocean heat transport (O'). We use anomalies averaged over years 85-115 for *dehose4x - 4xCO2* to assess differences between these experiments. As $C\,\frac{\partial T'}{\partial t}$ is an order of magnitude smaller than the surface heat flux terms (not shown), we can estimate the effect of ocean heat transport using the surface energy budget:

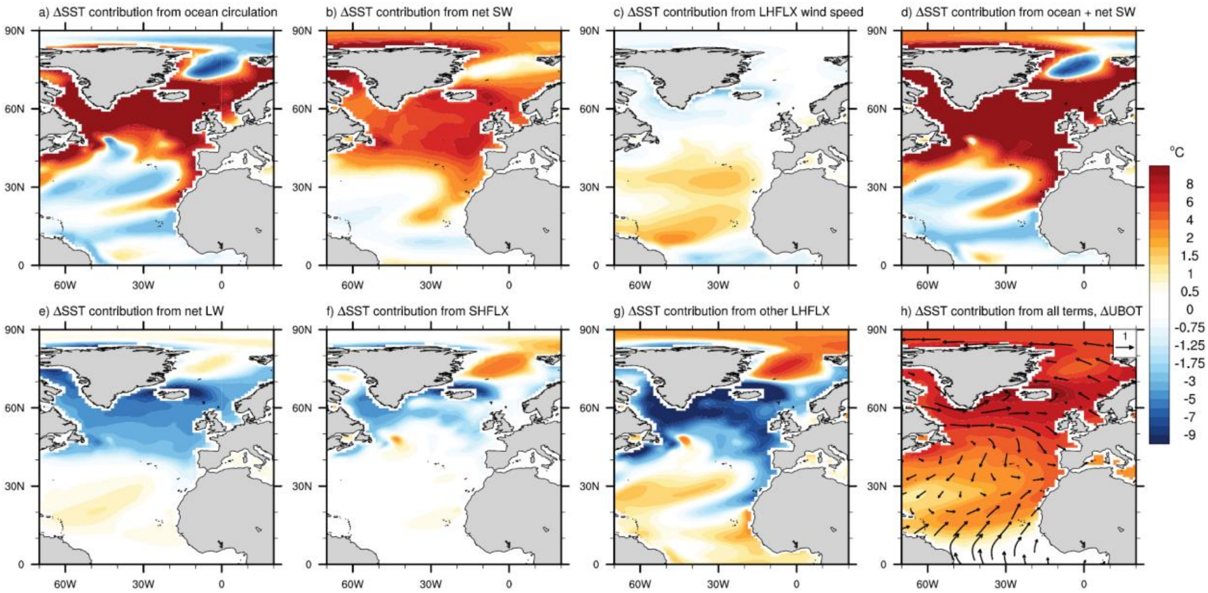

Figure 6. Mixed-layer budget decomposition of SST anomalies (°C) for *dehose4x – 4xCO2* due to anomalies in (a) ocean heat transport, (b) net shortwave radiation, (c) latent heat flux due to near-surface wind anomalies, (d) the sum of a) and b), (e) net longwave radiation, (f) sensible heat flux, (g) latent heat flux due to anomalies in near-surface relative humidity, air-sea temperature gradient, and a residual term, and (h) the sum of all terms, with arrows for near-surface horizontal wind anomalies (m/s).

$$O' = -(Q'_{SW} + Q'_{LW} + Q'_{SH} + Q'_{LH})\,. \qquad (4)$$

As detailed in Luongo et al. (2023), we substitute a bulk formula for the latent heat flux due to evaporation and use this to decompose latent heat flux anomalies due to Newtonian cooling of the surface and anomalies in near-surface wind (*W*), relative humidity (*RH*), the air-sea temperature gradient (*S*), and a residual term (*Res*). This allows for a diagnostic decomposition of contributions from different terms in the surface energy budget to SST differences for *dehose4x - 4xCO2*:

$$T' = T'_O + T'_{SW} + T'_{LW} + T'_{SH} + T'_{LH,W} + T'_{LH,RH} + T'_{LH,S} + T'_{LH,Res}\,. \qquad (5)$$

The three largest terms that increase North Atlantic warming with a stronger AMOC are ocean heat transport T'_O, net shortwave radiation T'_{SW}, and latent heat flux due to near-surface wind anomalies $T'_{LH,W}$ (Figure 6a-c). Ocean heat transport dominates, warming the surface particularly in the extratropical North Atlantic (Figure 6a). Cloud feedbacks amplify this effect, as warmer SSTs reduce cloud cover and increase shortwave absorption at the surface (Figure 6b). However, these two terms alone would cool most of the tropical Atlantic (Figure 6d); a positive wind-evaporation-SST (WES) feedback (Xie and Philander, 1994) is critical for extending warming to the tropics (Figure 6c).

A stronger AMOC weakens the climatological subtropical high, reducing near-surface wind speed (Figure 6h) and evaporative cooling in the subtropical and tropical North Atlantic. This southwestward propagation of positive SST anomalies in the tropical Atlantic via the WES feedback, here identified in response to AMOC differences, has also been found as part of a leading mode of variability in the North Atlantic, the Atlantic Meridional Mode (e.g., Amaya et al., 2017; Chang et al., 1997). Evaporative cooling in the tropical North Atlantic is further reduced (Figure 6g) by increased near-surface relative humidity associated with the northward ITCZ shift (Figure S11d) and by a weakened air-sea temperature gradient in the eastern deep tropics (Figure S11h). An increase in net longwave radiation (Figure 6e) due to more-positive water vapor and high-cloud feedbacks warms the tropical North Atlantic by a smaller amount than the WES feedback.

In summary, a mixed-layer heat budget shows that a stronger AMOC in *dehose4x* compared to *4xCO2* warms the North Atlantic primarily by reducing ocean heat uptake in the extratropics. A more-positive shortwave cloud feedback amplifies this warming, and a positive WES feedback extends it to the tropical North Atlantic. The WES feedback plays a key role not only for the North Atlantic but also for the global northern tropics, where thermally driven, southerly near-surface wind anomalies are redirected eastward by the Coriolis effect to weaken the trade winds, reduce evaporative cooling, and enhance sea-surface warming (Figure S11c,j).

f) Correlations of climate feedbacks with the AMOC decline across CMIP6 models

We have shown that the degree of AMOC decline in a single model mediates global climate feedbacks, particularly the North Atlantic shortwave cloud feedback. Do similar feedback differences arise from the intermodel spread in AMOC across CMIP6 models? To investigate this, we calculate climate feedbacks for each CMIP6 model in the same way as described for CESM2, using a regression of local TOA radiation anomalies against global-mean near-surface warming for the first 115 years of each CO_2 quadrupling experiment compared to the preindustrial control. We regress these feedbacks against anomalies in AMOC strength (averaged over years 85-115) across CMIP6 models, and we scale this regression (in W m^{-2} K^{-1} Sv^{-1}) by the difference in AMOC strength (in Sv) for the CESM2 *dehose4x* – *4xCO2* experiments for comparison (in W m^{-2} K^{-1} Figure 7b-h). Similarly, we regress near-surface warming averaged over years 85-115 against AMOC anomalies across

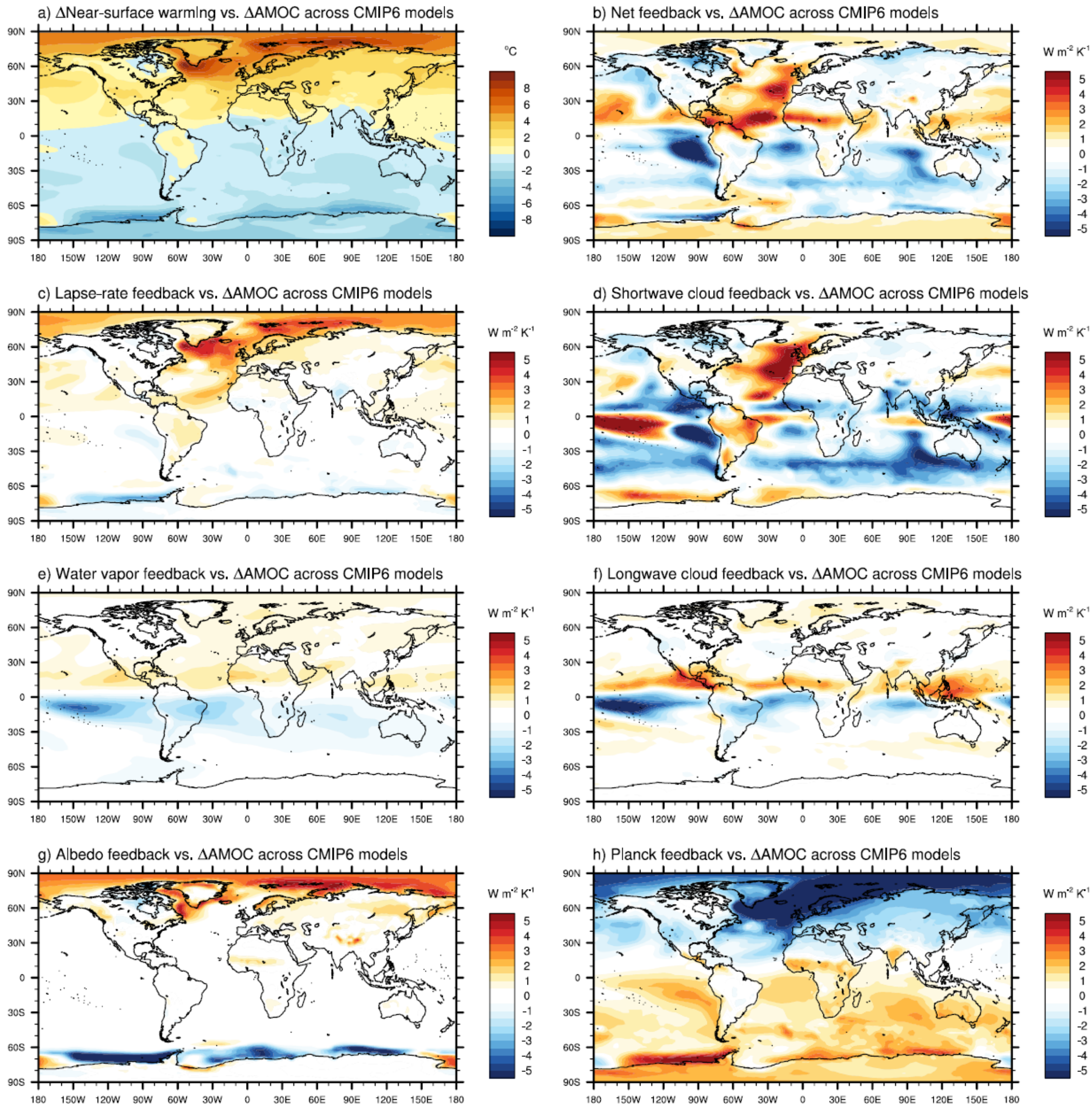

Figure 7. (a) Near-surface warming (°C) anomalies averaged over years 85-115 after CO_2 quadrupling and (b-h) climate feedbacks for the *abrupt4xCO2 – piControl* CMIP6 experiments, all regressed against the anomaly in AMOC strength averaged over years 85-115 after CO_2 quadrupling across CMIP6 models and scaled by the CESM2 *dehose4x – 4xCO2* anomaly in AMOC strength. Small residual term is shown in Figure S2b.

CMIP6 models and scale by the difference in AMOC strength for the *dehose4x – 4xCO2* experiments (Figure 7a).

We find similar relationships between the AMOC decline and climate feedbacks across CMIP6 models (Figure 7) as in our CESM2 experiments (Figure 3). Feedback changes in the North Atlantic for models with a stronger AMOC are dominated by less-negative shortwave cloud and lapse-rate feedbacks (Figure 7c,d), with similar patterns of anomalies as in CESM2. As in CESM2, a weaker AMOC decline (a stronger AMOC) across CMIP6 models is correlated with more-positive water vapor and longwave cloud feedbacks in the northern tropics due to a northward ITCZ shift, with an opposite response in the southern tropics (Figure 7e,f).

One key difference between the CESM2 experiments and correlations across CMIP6 models is that across CMIP6, models with a stronger AMOC produce more-positive lapse-rate and albedo feedbacks in the Arctic (Figure 7c,g). In contrast, a stronger AMOC in the CESM2 experiments produces more-negative Arctic lapse-rate and albedo feedbacks (Figure 3c,g). This difference likely results from sea ice differences. Across CMIP6, models with a stronger AMOC produce more sea-ice loss that supports more-positive albedo and lapse-rate feedbacks. However, in CESM2, the *dehose4x* experiment with a stronger AMOC produces an ice-free Arctic, crossing a threshold that precludes these positive sea-ice feedbacks, while *4xCO2* continues to lose sea ice throughout the experiment. As a result, our CESM2 experiments may underestimate the impact of intermodel spread in AMOC on Arctic warming in CMIP6.

Another difference is that CMIP6 models with a stronger AMOC tend to produce more-negative shortwave cloud feedbacks in the Southern Hemisphere (Figure 7d) in eastern tropical ocean basins and across the Southern Ocean than found in the CESM2 experiments (Figure 3d). This could reflect a larger low-cloud sensitivity to AMOC-induced surface cooling across CMIP6 models than in CESM2. Alternatively, this regression may reflect that more-negative cloud feedbacks in CMIP6 produce, rather than result from, a stronger AMOC. Our CESM2 experiments isolate the impact of AMOC on climate feedbacks, whereas regression across CMIP6 also reflects the impact of climate feedbacks on AMOC.

Lastly, we show area averages for the North Atlantic shortwave cloud, lapse-rate, and net feedbacks plotted against the AMOC decline for CMIP6 *4xCO2* experiments and for the CESM2 *4xCO2* and *dehose4x* experiments, all compared to *piControl* experiments (Figure 8). We include another data point for an intermediary CESM2 experiment that is identical to *dehose4x*, but with a .25 Sv dehosing (rather than .5 Sv). As seen in Figure 7, models with a weaker AMOC decline produce less-negative shortwave cloud, lapse-rate and net feedbacks in the North Atlantic. Moreover, a similar slope across CESM2 experiments as across CMIP6 models indicates that the sensitivity of North Atlantic feedbacks to the AMOC decline is comparable between our CESM2 experiments and other CMIP6 models.

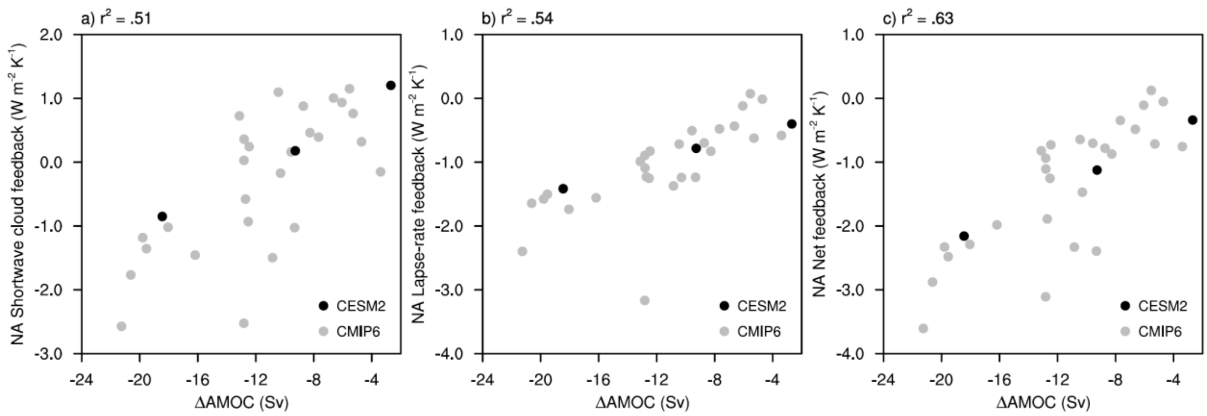

Figure 8. AMOC decline (Sv) for the *abrupt4xCO2 – piControl* CMIP6 experiments (grey dots) and for CESM2 abrupt CO_2 quadrupling experiments with no dehosing, a .25 Sv dehosing, and a .5 Sv dehosing (black dots from left to right), averaged over years 85-115 and plotted against (a) the shortwave cloud feedback, (b) the lapse-rate feedback, and (c) the net feedback for the North Atlantic from 15-60°N and 0-60°W (W m^{-2} K^{-1}).

In summary, we find similar relationships between the AMOC decline and climate feedbacks in CMIP6 regressions as in our CESM2 experiments, suggesting that our experiments are relevant for understanding AMOC impacts across CMIP6. These results are particularly interesting for the shortwave cloud feedback, which is also impacted by model differences in cloud physics. While many additional factors impact climate feedbacks, these results imply a key role for AMOC in mediating feedback differences across CMIP6 models.

g) Role of the North Atlantic region for global feedback change

To understand how the AMOC decline impacts the net global feedback, we have focused on the North Atlantic region, which shows the largest anomalies in local feedbacks for the *dehose4x – 4xCO2* experiments. However, the AMOC decline also influences warming beyond the North Atlantic, and past research suggests that the global feedback is most sensitive to SSTs in the tropical Pacific (Dong et al., 2019; Zhou et al., 2017). This raises the question: to what extent can AMOC-induced changes in the global feedback be explained by SST changes in the North Atlantic, as opposed to other regions?

To estimate the relative role of North Atlantic SSTs for global feedback changes, we use a Green's function approach, which allows us to reconstruct global changes in TOA radiation, near-surface warming, and the net climate feedback that result from local SST changes. We apply atmospheric Green's functions developed for CESM2 by Duffy et al. (*in prep.*) using +2K SST-patch experiments, following the Green's Function Model Intercomparison Project (GFMIP) protocol described in Bloch-Johnson et al. (2024). Green's functions estimate the sensitivity of global anomalies in TOA radiation and near-surface

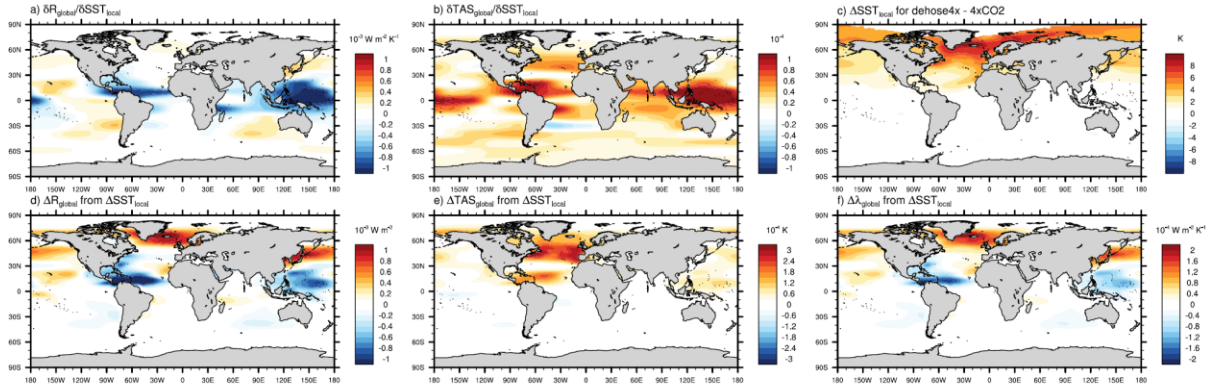

Figure 9. Green's functions for (a) global TOA radiative sensitivity ($\delta R_{global}/\delta SST_{local}$; W m^{-2} K^{-1}) and (b) global near-surface temperature sensitivity ($\delta TAS_{global}/\delta SST_{local}$) to local SST anomalies. (c) Local SST anomalies for the *dehose4x – 4xCO2* experiments averaged over years 85-115 and (d,e) their product with the Green's functions in a,b) to reconstruct (d) TOA radiation anomalies (W m^{-2}) and (e) near-surface temperature anomalies (K) for the *dehose4x – 4xCO2* experiments. (f) The change in global feedback resulting from local SST anomalies for *dehose4x – piControl* compared to *4xCO2 – piControl* experiments.

temperature to local SST anomalies ($\frac{\delta R_{global}}{\delta SST_i}$ and $\frac{\delta T_{global}}{\delta SST_i}$, respectively). Consistent with Green's functions developed for other models (Bloch-Johnson et al., 2024), the CESM2 Green's functions show the largest global radiative and warming sensitivity to SST in the western Pacific, and relatively small global sensitivity to SST in the North Atlantic (Figure 9a,b).

We multiply these sensitivities by local SST differences for *dehose4x - 4xCO2* in each year (ΔSST_i) to estimate each grid point's contribution to global-mean differences in TOA radiation $\left(\Delta R_{global_i}\right)$ and near-surface warming $\left(\Delta T_{global_i}\right)$, and we sum over all gridpoints to estimate the total change in ΔR_{global} and ΔT_{global}:

$$\Delta R_{global} = \sum_i \Delta R_{global_i} = \sum_i \frac{\delta R_{global}}{\delta SST_i} \Delta SST_i \, , \tag{6}$$

$$\Delta T_{global} = \sum_i \Delta T_{global_i} = \sum_i \frac{\delta T_{global}}{\delta SST_i} \Delta SST_i \, . \tag{7}$$

Averages over years 85-115 for ΔSST_i, ΔR_{global_i}, and ΔT_{global_i} are shown in Figure 9c-e. We add the Green's reconstructions of ΔR_{global} and ΔT_{global} for *dehose4x - 4xCO2* to the actual anomalies in ΔR_{global} and ΔT_{global} for *4xCO2 - piControl* to reconstruct anomalies in ΔR_{global} and ΔT_{global} for *dehose4x – piControl* (Figure S12). As discussed below, this allows for more accurate reconstructions than directly reconstructing anomalies for *dehose4x – piControl*. These reconstructions of ΔR_{global} and ΔT_{global} for *dehose4x – piControl* produce a reasonable approximation of the actual global anomalies, although they slightly underestimate near-surface warming.

Discrepancies between Green's function reconstructions and actual anomalies in global-mean TOA radiation and near-surface temperature may arise from applying Green's functions to fully-coupled rather than atmosphere-only experiments. In addition, Green's function reconstructions may introduce error by linearly summing the responses to regional SST forcings that induce larger changes in atmospheric circulation and convection (particularly in the tropics) than the actual response to more spatially-uniform anomalies (Dong et al., 2019). These Green's functions also exclude the impact of anomalies in sea-ice concentration on TOA radiation and near-surface temperature. We reduce these errors due to nonlinearities and sea-ice impacts by applying Green's functions to the *dehose4x – 4xCO2* difference (as opposed to *dehose4x - piControl* and *4xCO2 – piControl*), as both experiments have very little sea ice and have temperature differences that are largest in the extratropics.

Following Dong et al. (2019) and Zhou et al. (2017), we approximate the global feedback, $\lambda_{global} = (\Delta R_{global} - F)/\Delta T_{global}$, again setting F = 9.74 W m^{-2} K^{-1}. The Green's function reconstruction captures +0.08 W m^{-2} K^{-1} of the actual +0.11 W m^{-2} K^{-1} increase in global feedback for *dehose4x – piControl* compared to *4xCO2 – piControl*, averaged over years 85-115. We find qualitatively similar results when defining the feedback using regression, but use division here for consistency with the Green's function literature and for a better fit between reconstructed and actual feedback changes.

We calculate the contribution of different grid points or regions *i* to the total feedback change as:

$$\Delta\lambda_{i,\, dehose4x-4xCO2} = \frac{\Delta R_{global_{i,dehose4x-4xCO2}} + \Delta R_{global_{4xCO2-piControl}} - ERF}{\Delta T_{global_{i,dehose4x-4xCO2}} + \Delta T_{global_{4xCO2-piControl}}} - \lambda_{4xCO2-piControl}\,, \qquad (8)$$

where $\lambda_{4xCO2-piControl} = \frac{\Delta R_{global_{4xCO2-piControl}} - ERF}{\Delta T_{global_{4xCO2-piControl}}}$ is the actual net feedback for *4xCO2 – piControl*. Applying Equation 8 to the North Atlantic basin (0-60°W, north of 0°N), we find that North Atlantic SST changes alone reproduce the total +0.08 W m^{-2} K^{-1} increase in the reconstructed global feedback for *dehose4x – piControl* compared to *4xCO2– piControl*. We also use Equation 8 to calculate the contribution of AMOC-induced SST changes at each grid point to changes in the global feedback (Figure 9f). Figure 9f illustrates that a less-negative global feedback with a stronger AMOC is primarily driven by increased warming in the extratropical North Atlantic region. Extratropical North Pacific warming also produces a less-negative global feedback. As shown in Section 3c, warmer SSTs in both regions weaken the local inversion strength and low-cloud cover to support a more-positive shortwave cloud feedback.

In contrast, warming in the tropical western Pacific and Atlantic is effectively damped by a more-negative global feedback. Surface warming in these regions is communicated vertically by deep convection to the upper troposphere and then horizontally throughout the tropics by gravity waves, strengthening non-local inversions and negative shortwave cloud feedbacks (e.g., Williams et al., 2023). This analysis suggests that increased local warming in the tropical Atlantic induced by the WES feedback actually damps global-mean warming. Despite larger radiative sensitivities to SSTs in tropical regions (Figure 9a), the global feedback is impacted most by the extratropical North Atlantic (Figure 9f) because this region experiences the largest SST anomalies in response to AMOC changes (Figure 9c).

4. Summary and Conclusions

We use novel experiments in a state-of-the-art climate model to examine how the considerable model uncertainty in projections of AMOC weakening impacts uncertainty in near-future warming. Imposing the intermodel spread in AMOC decline within a single model, CESM2, reproduces more than 20% of the total intermodel spread in near-future warming across CMIP6, averaged over years 85-115 in CO_2-quadrupling experiments. A simple energy-balance model indicates that changes in ocean heat uptake and climate feedbacks in these experiments contribute approximately equally to the near-surface warming response to AMOC differences.

A weaker AMOC decline, resulting in a stronger AMOC, yields greater northward ocean heat transport that warms SSTs, particularly in the extratropical North Atlantic. Warmer SSTs reduce lower tropospheric stability, dissipating low clouds and allowing for greater absorbed shortwave radiation in a more-positive shortwave cloud feedback. In response to weakened winds in the subtropical North Atlantic and global northern tropics, reduced evaporative cooling extends warming to lower latitudes in a positive wind-evaporation-SST feedback. We quantify these effects using a radiative feedback decomposition, a cloud-controlling factor analysis, and a mixed-layer heat budget.

Furthermore, we use Green's functions to illustrate that a less-negative global feedback with a stronger AMOC results primarily from sea-surface warming in the extratropical North Atlantic. Moreover, we find similar changes in ocean heat uptake and climate feedbacks correlated with the AMOC decline across CMIP6 models as in our CESM2 experiments. This consistency suggests that our experiments within a single model are relevant for understanding AMOC impacts on intermodel spread across CMIP6.

One caveat to this analysis is that the sensitivity of climate feedbacks to AMOC in CESM2 may not be representative of other climate models. CESM2 is known to have a too-positive shortwave cloud feedback particularly in the Southern Hemisphere due to issues with cloud microphysical parameterizations (Shaw et al., 2022; Zhu et al., 2022). A more realistic cloud microphysical scheme may produce differences in the cloud feedback and warming response to the AMOC decline. However, as noted above, we find similar feedback changes associated with the AMOC decline across CMIP6 models as in our CESM2 experiments. Further, in our cloud controlling factor analysis, observational cloud radiative sensitivities produce similar cloud feedback changes as the CESM2 radiative sensitivities (Figure S7-10). This analysis indicates that a stronger AMOC produces a robust increase in the North Atlantic shortwave low-cloud feedback (and a decrease in the Southern Hemisphere shortwave low-cloud feedback) by changing sea-surface temperatures and inversion strengths.

CESM2 also simulates insufficient sea-ice cover in present and future climates (Kay et al., 2022). As a result, CMIP6 models with more mean-state sea ice may show a larger effect of the AMOC on Arctic feedbacks and warming (Bellomo and Mehling, 2024), as suggested by regressions of Arctic feedbacks against the AMOC decline across CMIP6 models (Figure 7). We plan to explore the role of AMOC for uncertainty in Arctic warming as mediated by sea ice in a follow-up study. Additionally, coupled interactions between ocean circulation and climate feedbacks complicate assessments of how each mediates the surface warming response to AMOC changes; we plan to apply more idealized experiments to address this in future work.

This study contributes novel mechanistic insight on how the AMOC decline impacts climate feedbacks, and demonstrates that we need to understand both feedback changes and ocean circulation changes to understand AMOC impacts on near-future warming. We also quantify for the first time the extent to which uncertainty in the AMOC decline across CMIP6 models may impact uncertainty in global warming. Others have suggested that constraining the mean-state AMOC strength using observations is a promising avenue for constraining AMOC projections (Bonan et al., submitted; Lin et al., 2023; Weijer et al., 2020). Given the sizeable effect of uncertainty in the AMOC decline on uncertainty in global warming, our results suggest that constraining AMOC projections may substantially reduce global warming uncertainty.

Acknowledgments.

We thank Aixue Hu for sharing source modifications to implement freshwater forcing in CESM2. We thank Margaret Duffy for sharing Green's functions for CESM2, and we thank Sarah Kang and Paolo Ceppi for sharing cloud radiative sensitivities for CESM2. L.C.H. was supported by the NOAA Climate and Global Change Postdoctoral Fellowship Program, administered by UCAR's Cooperative Programs for the Advancement of Earth System Science (CPAESS) under award #NA21OAR4310383 and #NA23OAR4310383B. N.J.L. was funded by NSF Grant OCE-2023520. M.T.L. was supported by NASA FINESST Fellowship 80NSSC22K1528. This work was also supported by NSF grant OCE-2048590.

Data Availability Statement.

Output from the *piControl* and *abrupt-4xCO2* experiments in CESM2 and other CMIP6 models can be found in the Earth System Grid Federation (ESGF) repository at https://esgf-node.llnl.gov/projects/esgf-llnl/. Model output from the CESM2 *dehose4x* experiment will be publicly available at https://doi.org/10.5281/zenodo.14219338 upon publication.

REFERENCES

Amaya, D. J., M. J. DeFlorio, A. J. Miller, and S.-P. Xie, 2017: WES feedback and the Atlantic Meridional Mode: observations and CMIP5 comparisons. *Clim Dyn,* **49**, 1665–1679, https://doi.org/10.1007/s00382-016-3411-1.

Armour, K. C., C. M. Bitz, and G. H. Roe, 2013: Time-Varying Climate Sensitivity from Regional Feedbacks. *J. Climate*, **26**(13), 4518-4534, https://doi.org/10.1175/JCLI-D-12-00544.1.

Bellomo, K., M. Angeloni, S. Corti, and J. von Hardenberg, 2021: Future climate change shaped by inter-model differences in Atlantic meridional overturning circulation response. *Nat. Comm.*, **12**, 3659, https://doi.org/10.1038/s41467-021-24015-w.

Bellomo, K., and Mehling, O., 2024: Impacts and state-dependence of AMOC weakening in a warming climate. *Geophysical Research Letters*, 51, e2023GL107624, https://doi.org/10.1029/2023GL107624.

Bitz, C. M., K. M. Shell, P. R. Gent, D. A. Bailey, G. Danabasoglu, K. C. Armour, M. M. Holland, and J. T. Kiehl, 2012: Climate Sensitivity of the Community Climate System Model, Version 4. *J. Climate*, **25**, 3053–3070, https://doi.org/10.1175/JCLI-D-11-00290.1.

Bloch-Johnson, J., and Coauthors, 2024: The Green's function model intercomparison project (GFMIP) protocol. *Journal of Advances in Modeling Earth Systems*, **16**, e2023MS003700, https://doi.org/10.1029/ 2023MS003700.

Bonan, D., Thompson, A., Schneider, T., Zanna, L., Armour, K., and Sun, S. (submitted 2024): Constraints imply limited future weakening of Atlantic meridional overturning circulation.

Caldwell, P. M., Zelinka, M. D., Taylor, K. E., & Marvel, K, 2016: Quantifying the sources of intermodel spread in equilibrium climate sensitivity. *Journal of Climate*, **29**(2), 513–524, https://doi.org/10.1175/jcli-d-15-0352.1.

Ceppi, P. & Nowack, P., 2021: Observational evidence that cloud feedback amplifies global warming. *Proc. Natl Acad. Sci. USA,* **118**, e2026290118.

Chang, P., L. Ji & H. Li, 1997: A decadal climate variation in the tropical Atlantic Ocean from thermodynamic air-sea interactions. *Nature*, **385**, 516–518, https://doi.org/10.1038/385516a0.

Danabasoglu, G., Lamarque, J.-F., Bacmeister, J., Bailey, D. A., DuVivier, A. K., Edwards, J., et al., 2020: The Community Earth System Model Version 2 (CESM2). *Journal of Advances in Modeling Earth Systems*, **12**, e2019MS001916, https://doi.org/10.1029/2019MS001916.

Dong, Y., C. Proistosescu, K. C. Armour, and D. S. Battisti, 2019: Attributing Historical and Future Evolution of Radiative Feedbacks to Regional Warming Patterns using a Green's Function Approach: The Preeminence of the Western Pacific. *J. Climate*, **32**, 5471–5491, https://doi.org/10.1175/JCLI-D-18-0843.1.

Donohoe, A., K. C. Armour, A. G. Pendergrass, and D. S. Battisti, 2014: Shortwave and longwave radiative contributions to global warming under increasing CO_2. *Proceedings of the National Academy of Sciences*, **111**(47), 16700 -16705, https://doi.org/10.1073/pnas.1412190111.

Geoffroy, O., D. Saint-Martin, and A. Ribes, 2012: Quantifying the sources of spread in climate change experiments. *Geophys. Res. Lett.*, **39**, L24703, https://doi.org/10.1029/2012GL054172.

Geoffroy, O., D. Saint-Martin, D. J. L. Olivié, A. Voldoire, G. Bellon, and S. Tytéca, 2013: Transient Climate Response in a Two-Layer Energy-Balance Model. Part I: Analytical Solution and Parameter Calibration Using CMIP5 AOGCM Experiments. *J. Climate*, **26**(6), 1841-1857, https://doi.org/10.1175/JCLI-D-12-00195.1.

Gregory, J. M., and J. F. B. Mitchell, 1997: The climate response to CO2 of the Hadley Centre coupled AOGCM with and without flux adjustment. *Geophys. Res. Lett.*, **24**, 1943–1946.

Gregory, J. M., and Coauthors, 2005: A model intercomparison of changes in the Atlantic thermohaline circulation in response to increasing atmospheric CO_2 concentration. *Geophys. Res. Lett.*, **32**, L12703, https://doi.org/10.1029/2005GL023209.

Gregory, J. M., and P. M. Forster, 2008: Transient climate response estimated from radiative forcing and observed temperature change. *J. Geophys. Res.*, **113**, D23105, doi:10.1029/2008JD010405.

Gregory, J. M., and Coauthors, 2024: A new conceptual model of global ocean heat uptake. *Clim. Dyn.*, **62**, 1669–1713, https://doi.org/10.1007/s00382-023-06989-z.

Huang, Y., Y. Xia, Y., and X. Tan, 2017: On the Pattern of CO2 Radiative Forcing and Poleward Energy Transport. *J. Geophys. Res. Atmos.*, **122**, 10578–10593, doi:10.1002/2017JD027221.

He, J., M. Winton, G. Vecchi, L. Jia, and M. Rugenstein, 2017: Transient Climate Sensitivity Depends on Base Climate Ocean Circulation. *J. Climate*, **30**(4), 1493-1504, https://doi.org/10.1175/JCLI-D-16-0581.1.

Hunke, E. C, W. H. Lipscomb, A. K. Turner, N. Jeffery, and S. Elliott, 2015: CICE: The Los Alamos Sea Ice Model. Documentation and Software User's Manual. Version 5.1. *T-3 Fluid Dynamics Group*, Los Alamos National Laboratory, Tech. Rep. LA-CC-06-012.

IPCC, 2021: *Climate Change 2021: The Physical Science Basis. Contribution of Working Group I to the Sixth Assessment Report of the Intergovernmental Panel on Climate Change* [Masson-Delmotte, V., P. Zhai, A. Pirani, S.L. Connors, C. Péan, S. Berger, N. Caud, Y. Chen, L. Goldfarb, M.I. Gomis, M. Huang, K. Leitzell, E. Lonnoy, J.B.R. Matthews, T.K. Maycock, T. Waterfield, O. Yelekçi, R. Yu, and B. Zhou (eds.)]. Cambridge University Press, Cambridge, United Kingdom and New York, NY, USA.

Jackson, L. C., and Coauthors, 2023: Understanding AMOC stability: the North Atlantic Hosing Model Intercomparison Project. *Geosci. Model Dev.*, **16**, 1975–1995, https://doi.org/10.5194/gmd-16-1975-2023.

Kang, S. M., I. M. Held, D. M. W. Frierson, and M. Zhao, 2008: The Response of the ITCZ to Extratropical Thermal Forcing: Idealized Slab-Ocean Experiments with a GCM. *J. Climate*, **21**, 3521–3532, https://doi.org/10.1175/2007JCLI2146.1.

Kang, S.M., Ceppi, P., Yu, Y. *et al.*, 2023: Recent global climate feedback controlled by Southern Ocean cooling. *Nat. Geosci.*, **16**, 775–780, https://doi.org/10.1038/s41561-023-01256-6.

Kay, J. E., and Coauthors, 2022: Less surface sea ice melt in the CESM2 improves Arctic sea ice simulation with minimal non-polar climate impacts. *J. Adv. Model. Earth Syst.*, **14**, e2021MS002679, https://doi.org/10.1029/2021MS002679.

Kostov, Y., K. C. Armour, and J. Marshall, 2014: Impact of the Atlantic meridional overturning circulation on ocean heat storage and transient climate change. *Geophys. Res. Lett.*, **41**, 2108– 2116, https://doi.org/10.1002/2013GL058998.

Lawrence, D. M., and Coauthors, 2019: The Community Land Model Version 5: Description of new features, benchmarking, and impact of forcing uncertainty. *Journal of Advances in Modeling Earth Systems*, **11**, 4245–4287, https://doi.org/10.1029/2018MS001583.

Li, H. Y., M. S. Wigmosta, H. Wu, M. Y. Huang, Y. H. Ke, A. M. Coleman, and L. R. Leung, 2013: A physically based runoff routing model for land surface and Earth system models. *J. Hydrometeorology*, **14**, 808–828, https://doi.org/10.1175/Jhm-D-12-015.1.

Lin, Y., B. E. J. Rose, and Y. Hwang, 2023: Mean State AMOC Affects AMOC Weakening through Subsurface Warming in the Labrador Sea. *J. Climate*, **36**, 3895–3915, https://doi.org/10.1175/JCLI-D-22-0464.1.

Lipscomb, W. H., and Coauthors, 2019: Description and evaluation of the Community Ice Sheet Model (CISM) v. 2.1. *Geoscientific Model Development*, **12**, 387–424, https://doi.org/10.5194/gmd-12-387-2019.

Liu, W., A. Fedorov, S.-P. Xie, and S. Hu, 2020: Climate impacts of a weakened Atlantic meridional overturning circulation in a warming climate. *Science Advances*, **6**, eaaz4876, https://doi.org/10.1126/sciadv.aaz4876.

Liu, G., F. Tagklis, T. Ito, T., and A. Bracco, 2024: Drivers of coupled climate model biases in representing Labrador Sea convection. *Clim Dyn*, **62**, 3337–3353, https://doi.org/10.1007/s00382-023-07068-z.

Luongo, M. T., Xie, S.-P., Eisenman, I., Hwang, Y.-T., & Tseng, H.-Y., 2023: A pathway for Northern Hemisphere extratropical cooling to elicit a tropical response. *Geophysical Research Letters*, 50, e2022GL100719, https://doi.org/10.1029/2022GL100719.

Lutsko, N. J., & M. Popp, 2019: Probing the sources of uncertainty in transient warming on different timescales. *Geophys. Res. Lett.*, **46**, 11367– 11377, https://doi.org/10.1029/2019GL084018.

Marshall, J., J. R. Scott, K. C. Armour, J.-M. Campin, M. Kelley, and A. Romanou, A., 2015: The ocean's role in the transient response of climate to abrupt greenhouse gas forcing. *Climate Dynamics*, **44**, 2287–2299, https://doi.org/10.1007/s00382-014-2308-0.

Myers, T.A., R. C. Scott, M. D. Zelinka, *et al.*, 2021: Observational constraints on low cloud feedback reduce uncertainty of climate sensitivity. *Nat. Clim. Chang.*, **11**, 501–507, https://doi.org/10.1038/s41558-021-01039-0.

Pendergrass, A. G., A. Conley, A., and F. M. Vitt, 2018: Surface and Top-Of-Atmosphere Radiative Feedback Kernels for CESM-CAM5. *Earth Syst. Sci. Data*, **10** (1), 317–324, doi:10.5194/essd-10-317-2018.

Raper, S. C. B., J. M. Gregory, and R. J. Stouffer, 2002: The Role of Climate Sensitivity and Ocean Heat Uptake on AOGCM Transient Temperature Response. *J. Climate*, **15**, 124–130, https://doi.org/10.1175/1520-0442(2002)015<0124:TROCSA>2.0.CO;2.

Rose, B. E. J., K. C. Armour, D. S. Battisti, N. Feldl, and D. D. B. Koll, 2014: The dependence of transient climate sensitivity and radiative feedbacks on the spatial pattern of ocean heat uptake. *Geophys. Res. Lett.*, **41**, https://doi.org/10.1002/2013GL058955.

Rugenstein, M. A. A., M. Winton, R. J. Stouffer, S. M. Griffies, and R. Hallberg, 2013: Northern High-Latitude Heat Budget Decomposition and Transient Warming. *J. Climate*, **26**(2), 609-621, https://doi.org/10.1175/JCLI-D-11-00695.1.

Shaw, J., McGraw, Z., Bruno, O., Storelvmo, T., and Hofer, S., 2022: Using satellite observations to evaluate model microphysical representation of Arctic mixed-phase clouds. *Geophys. Res. Lett.*, **49**, e2021GL096191, https://doi.org/10.1029/2021GL096191.

Shell, K. M., J. T. Kiehl, and C. A. Shields, 2008: Using the radiative kernel technique to calculate climate feedbacks in NCAR's Community Atmospheric Model. *J. Climate*, **21**, 2269–2282, https://doi.org/10.1175/2007JCLI2044.1.

Smith, R., and Coauthors, 2010: The Parallel Ocean Program (POP) reference manual, Ocean component of the Community Climate System Model (CCSM), LANL Tech. Report, LAUR-10-01853, 141 pp.

Smith, C. J., and Coauthors, 2020: Effective radiative forcing and adjustments in CMIP6 models. *Atmos. Chem. Phys.*, **20**, 9591–9618, https://doi.org/10.5194/acp-20-9591-2020.

Soden, B. J., I. M. Held, R. Colman, K. M. Shell, J. T. Kiehl, and C. A. Shield, 2008: Quantifying climate feedbacks using radiative kernels. *J. Climate*, **21**, 3504–3520, https://doi.org/10.1175/2007JCLI2110.1.

Trossman, D. S., J. B. Palter, T. M. Merlis, Y. Huang, and Y. Xia, 2016: Large-scale ocean circulation-cloud interactions reduce the pace of transient climate change. *Geophys. Res. Lett.*, **43**, 3935– 3943, https://doi.org/10.1002/2016GL067931.

Vellinga, M., and R. A. Wood, 2008: Impacts of thermohaline circulation shutdown in the twenty-first century. *Clim. Change*, **91**, 43–63, https://doi.org/10.1007/s10584-006-9146-y.

Weijer, W., W. Cheng, O. A. Garuba, A. Hu, and B. T. Nadiga, 2020: CMIP6 models predict significant 21st century decline of the Atlantic Meridional Overturning Circulation. *Geophys. Res. Lett.*, **47**, e2019GL086075, https://doi.org/10.1029/2019GL086075.

Williams, A. I. L., Jeevanjee, N., & Bloch-Johnson, J., 2023: Circus tents, convective thresholds, and the non-linear climate response to tropical SSTs. *Geophys. Res. Lett.*, **50**, e2022GL101499, https://doi.org/10.1029/2022GL101499.

Winton, M., 2003: On the Climatic Impact of Ocean Circulation. *J. Climate*, **16**, 2875–2889, https://doi.org/10.1175/1520-0442(2003)016<2875:OTCIOO>2.0.CO;2.

Winton, M., K. Takahashi, and I. M. Held, 2010: Importance of Ocean Heat Uptake Efficacy to Transient Climate Change. *J. Climate*, **23**, 2333–2344, https://doi.org/10.1175/2009JCLI3139.1.

Winton, M., S. M. Griffies, B. L. Samuels, J. L. Sarmiento, and T. L. Frölicher, 2013: Connecting Changing Ocean Circulation with Changing Climate. *J. Climate*, **26**, 2268-2278, https://doi.org/10.1175/JCLI-D-12-00296.1.

Xie, S.-P., C. Deser, G. A. Vecchi, J. Ma, H. Teng, and A. T. Wittenberg, 2010: Global warming pattern formation: Sea surface temperature and rainfall. *J. Climate*, **23**(4), 966–986, https://doi.org/10.1175/2009jcli3329.1.

Xie, S.-P., and S. G. H. Philander, 1994: A coupled ocean-atmosphere model of relevance to the ITCZ in the eastern Pacific. *Tellus*, **46**, 340–350.

Zelinka, M. D., T. A. Myers, D. T. McCoy, S. Po-Chedley, P. M. Caldwell, P. Ceppi, et al., 2020: Causes of Higher Climate Sensitivity in CMIP6 Models. *Geophys. Res. Lett.*, **47**, e2019GL085782, doi:10.1029/2019GL085782.

Zhang, R., and T. L. Delworth, 2005: Simulated Tropical Response to a Substantial Weakening of the Atlantic Thermohaline Circulation. *J. Climate*, **18**, 1853–1860, https://doi.org/10.1175/JCLI3460.1.

Zhang, R., S. M. Kang, and I. M. Held, 2010: Sensitivity of Climate Change Induced by the Weakening of the Atlantic Meridional Overturning Circulation to Cloud Feedback. *J. Climate*, **23**, 378–389, https://doi.org/10.1175/2009JCLI3118.1.

Zhou, C., M. D. Zelinka, and S. A. Klein, 2017: Analyzing the dependence of global cloud feedback on the spatial pattern of sea surface temperature change with a Green's function approach. *J. Adv. Model. Earth Syst.*, **9**, 2174–2189, doi:10.1002/2017MS001096.

Zhu, J., and Coauthors, 2022: LGM paleoclimate constraints inform cloud parameterizations and equilibrium climate sensitivity in CESM2. *J. Adv. Model. Earth Syst.*, **14**, e2021MS002776, https://doi.org/10.1029/2021MS002776.